Reinvestigating the level structure of ^{95}Mo: Coexistence of single-particle excitations and collective motions*

S. Y. Guo (郭思源)[1#] R. Guo (郭瑞)[2#] J. B. Lu (陆景彬)[1†] B. Ding (丁兵)[3,4‡] D. Chen (陈铎)[5]
H. Y. Ye (叶欢仪)[1] Z. Ren (任臻)[1] J. Li (李剑)[1] K. Y. Ma (马克岩)[1] S. Guo (郭松)[3,4] M. L. Liu (柳敏良)[3,4]
K. K. Zheng (郑宽宽)[3,4] G. S. Li (李广顺)[3,4] J. G. Wang (王建国)[3,4] Y. H. Qiang (强赟华)[3,4] Y. D. Fang (方永得)[3,4]
M. Y. Liu (刘梦瑶)[3,4] W. Q. Zhang (张文强)[3,4] F. F. Zeng (曾凡斐)[3,4] H. Huang (黄浩)[3,4] Q. B. Zeng (曾全波)[3,4]
Y. Zheng (郑云)[6] T. X. Li (李天晓)[6] S. Y. Wang (王守宇)[7] C. Liu (刘晨)[7] X. C. Han (韩星池)[7] X. Xiao (肖骁)[7]
L. Mu (穆琳)[7] W. Z. Xu (许文政)[7] H. F. Bai (白洪斐)[7] Y. J. Li (李英健)[7] X. D. Wang (王旭东)[7]
L. Zhu (祝霖)[7] Y. H. Wu (吴义恒)[8]

[1]College of Physics, Jilin University, Changchun 130012, China
[2]Institute of Modern Physics, Chinese Academy of Sciences, Lanzhou 730000, China
[3]State Key Laboratory of Heavy Ion Science and Technology, Institute of Modern Physics, Chinese Academy of Sciences, Lanzhou 730000, China
[4]School of Nuclear Science and Technology, University of Chinese Academy of Science, Beijing 100049, China
[5]School of Physics, Harbin Institute of Technology, Harbin 150001, China
[6]China Institute of Atomic Energy, Beijing 102413, China
[7]Shandong Provincial Key Laboratory of Optical Astronomy and Solar-Terrestrial Environment, Institute of Space Sciences, Shandong University, Weihai 264209, China
[8]School of Electronic Engineering and Intelligent Manufacturing, AnQing Normal University, Anqing 246133, China

Abstract: Excited states of ^{95}Mo have been reinvestigated via the ^{87}Rb(^{12}C,1p3n)^{95}Mo fusion-evaporation reaction at a beam energy of 62 MeV. The level scheme of ^{95}Mo was enriched by the addition of 13 γ-ray transitions and 11 new levels, while the placements of 6 transitions were reassigned. Shell-model calculations with the GWBXG and SNET interactions were performed to reproduce parts of the observed level structure, providing relevant configuration information. Furthermore, a systematic analysis of the low-lying positive-parity yrast states was conducted for ^{95}Mo and its neighboring $N = 53$ isotones. In addition, three-dimensional tilted axis cranking covariant density functional theory (3DTAC-CDFT) calculations indicated weakly prolate deformation for ^{95}Mo. Combined with systematics, this result suggests that collectivity similar to that in neighboring nuclei such as ^{97,99,101}Mo may be presented in ^{95}Mo.

Keywords: γ-γ-γ coincidence measurement, level scheme, shell model, collective motion

DOI: 10.1088/1674-1137/ae457b **CSTR:** 32044.14.ChinesePhysicsC.50054002

I. INTRODUCTION

Nuclear structure studies in the vicinity of $Z \sim 40$ and $N \sim 50$ have attracted considerable attention in recent years. These investigations focus on a variety of intriguing phenomena, such as seniority conservation, cross-shell excitations, and exotic rotations [1–5]. In this nuclear region, many nuclei have near-spherical ground states, and their low-lying excitations are predominantly of single-particle character, well described by the shell model [2–4, 6]. As the neutron number increases from the $N = 50$ closed shell, the shapes of nuclei in this region gradually evolve from spherical to deformed.

For example, in the Mo isotopic chain in this nuclear region, the level structures of $^{92-94}$Mo predominantly exhibit single-particle excitations [7–9], whereas rotational-like structures have been observed in $^{97,99-101}$Mo [10–12]. For instance, the systematic observation of rotational-like sequences in ^{97,99,101}Mo has been interpreted as $\nu h_{11/2}$ decoupled bands, and theoretical calculations indicate a gradual increase in deformation for these nuclei [12]. Similar collective rotational structures have emerged sys-

Received 9 December 2025; Accepted 13 February 2026; Accepted manuscript online 14 February 2026

* Supported by the National Natural Science Foundation of China (U1867210, 12441506, 12375128, U2032211), the Major Science and Technology Projects in Gansu Province (24GD13GA005), and the Independent Deployment Project of State Key Laboratory of Heavy Ion Science and Technology

† E-mail: ljb@jlu.edu.cn
‡ E-mail: dbing@impcas.ac.cn
# These authors contributed equally as the first authors

tematically in other odd-A nuclei (adjacent to the Mo isotopes) [12–16]. In particular, with increasing proton number, the negative-parity sequences in nuclei such as ^{101,102}Ru and ^{99,101}Pd have been proposed as antimagnetic rotational bands [5, 17–19], demonstrating the diversity of collective modes in this region. For the Mo isotopic chain, in the $N = 50$ closed-shell nucleus ^{92}Mo, the two valence protons in the $g_{9/2}$ orbital give rise to a seniority scheme, and an 8^+ isomer has been observed [1, 20]. With the addition of only one neutron, ^{93}Mo exhibits a particularly interesting structure, including a high-spin $21/2^+$ isomer [8, 21]. In ^{94}Mo, an 8^+ isomer is still present [22]; however, the level spacing from 0^+ to 8^+ does not decrease as rapidly with increasing spin as it does in ^{92}Mo.

The aforementioned description indicates that ^{95}Mo likely lies in the transitional region from spherical to deformed nuclei. Consequently, ^{95}Mo was selected as the subject of this study to explore the possible coexistence of single-particle excitations and collective motion. Investigations of the level structure of ^{95}Mo date back to early works. Initial investigations of its low-spin structure were performed via the ^{94}Zr(α,3n) reaction by Lederer *et al.* [22, 23] and via the ^{92}Zr(α,n) reaction by Meško *et al*. [24]. Subsequently, the low-spin structure of ^{95}Mo was also investigated via Coulomb excitation [25] and β decay [26], with the obtained results further enriching the low-spin level scheme [27]. In addition, several specific low-lying states in ^{95}Mo were established (these specific low-lying states were not observed in subsequent high-spin studies, nor in the present work). In 1998, Kharraja *et al*. investigated its high-spin states using the ^{65}Cu(^{36}S,α pn) reaction for the first time [28]. Subsequent investigations, including those by Chatterjee *et al*. in 2004 [29] using the ^{82}Se(^{18}O,3n) heavy-ion fusion-evaporation reaction and by Zhang *et al.* in 2009 [9] using the ^{16}O(^{82}Se,3n) reaction, further enriched the high-spin level scheme of ^{95}Mo.

The present study further extends the level structure of ^{95}Mo via the ^{87}Rb(^{12}C,1p3n) fusion-evaporation reaction. This paper is organized as follows: The experimental details are described in Sec. II. The analysis of the experimental data and the corresponding results are presented in Sec. III. Shell-model and three-dimensional tilted axis cranking covariant density functionaltheory (3DTAC-CDFT) calculations are discussed in Secs. IV.A and IV.B, respectively. Finally, a summary of the present study is provided in Sec. V.

II. EXPERIMENTAL DETAILS

The excited states of ^{95}Mo were populated via the ^{87}Rb(^{12}C,1p3n)^{95}Mo nuclear reaction. The ^{12}C beam with an energy of 62 MeV was delivered by the Sector Focusing Cyclotron at the Heavy Ion Research Facility in Lanzhou (HIRFL). In this experiment, the target a ^{87}RbCl foil, with a thickness of 4.2 mg/cm^2, was used as the target. Given its hygroscopic nature, it was capped on the front side with a 18 μg/cm^2 carbon foil and backed by an 8.7 mg/cm^2 foil of natural Pb, which served as the backing material. The emitted γ rays were detected using a multi-detector array, containing five clover detectors of the EXOGAM type [30] grouped into a ring at 90° and fourteen high-purity germanium (HPGe) detectors (with a relative efficiency of 70%) grouped into four rings at ±52° and ±26° relative to the beam axis. All the detectors were equipped with BGO anti-Compton shields. Energy and efficiency calibrations were performed using ^{60}Co, ^{133}Ba, and ^{152}Eu standard radioactive sources. The typical energy resolution was approximately 2.0−2.5 keV at the full width at half-maximum (FWHM) of the 1332.5-keV γ ray of ^{60}Co. A total of 1×10^9 γ-γ-γ coincidence events were recorded. These events were sorted into fully symmetrized matrices and cubes, which were subsequently analyzed off-line using the RADWARE [31] software package.

To extract multipolarity information of the γ rays, two asymmetric coincidence matrices were constructed. In these matrices, the y-axis utilized the γ rays detected at all angles, while the x-axis included γ rays detected under two conditions, ±26° and 90°. From these two matrices, the angular distribution asymmetry ratios, defined as $R_{\rm ADO} = I_\gamma(\pm26°)/I_\gamma(90°)$, were extracted from the γ-ray intensities $I_\gamma(26°$ and $-26°)$ and $I_\gamma(90°)$ in the coincidence spectra gated by the γ transitions (on the y-axis) of any multipolarity. For the present detector geometry and through comparison with γ rays of known polarity from this experiment, the $R_{\rm ADO}$ value for stretched quadrupole (or $\Delta J = 0$ dipole) transitions was ~ 1.4, whereas that for stretched pure dipole transitions was ~ 0.8.

III. EXPERIMENTAL RESULTS

The level scheme of ^{95}Mo, constructed in the present study, is shown in Fig. 1. This work extends and revises the level scheme of ^{95}Mo, adding 13 γ-ray transitions and 11 new levels, and reassigning the placements of 6 transitions. Notably, the 201.8-, 977.1-, 990.8-, 1078.2-, and 1310.8-keV transitions, which were observed in Ref. [29], have been confirmed in the present study. Their placements within the scheme have been reassigned based on the coincidence relationships observed in this study. The γ-ray energies, initial and final levels, intensities, and ADO ratios for ^{95}Mo, extracted from the current experiment, are listed in Table 1. An evaluation of the $R_{\rm ADO}$ values for the γ rays with known multipolarity in ^{95}Mo produced in the current experiment, as shown in Figs. 2, reveals $R_{\rm ADO}$ ~ 1.4 and ~ 0.8 for the stretched quadrupole and stretched dipole transitions, respectively. The spin-parity assignments for ^{95}Mo, based on the ADO

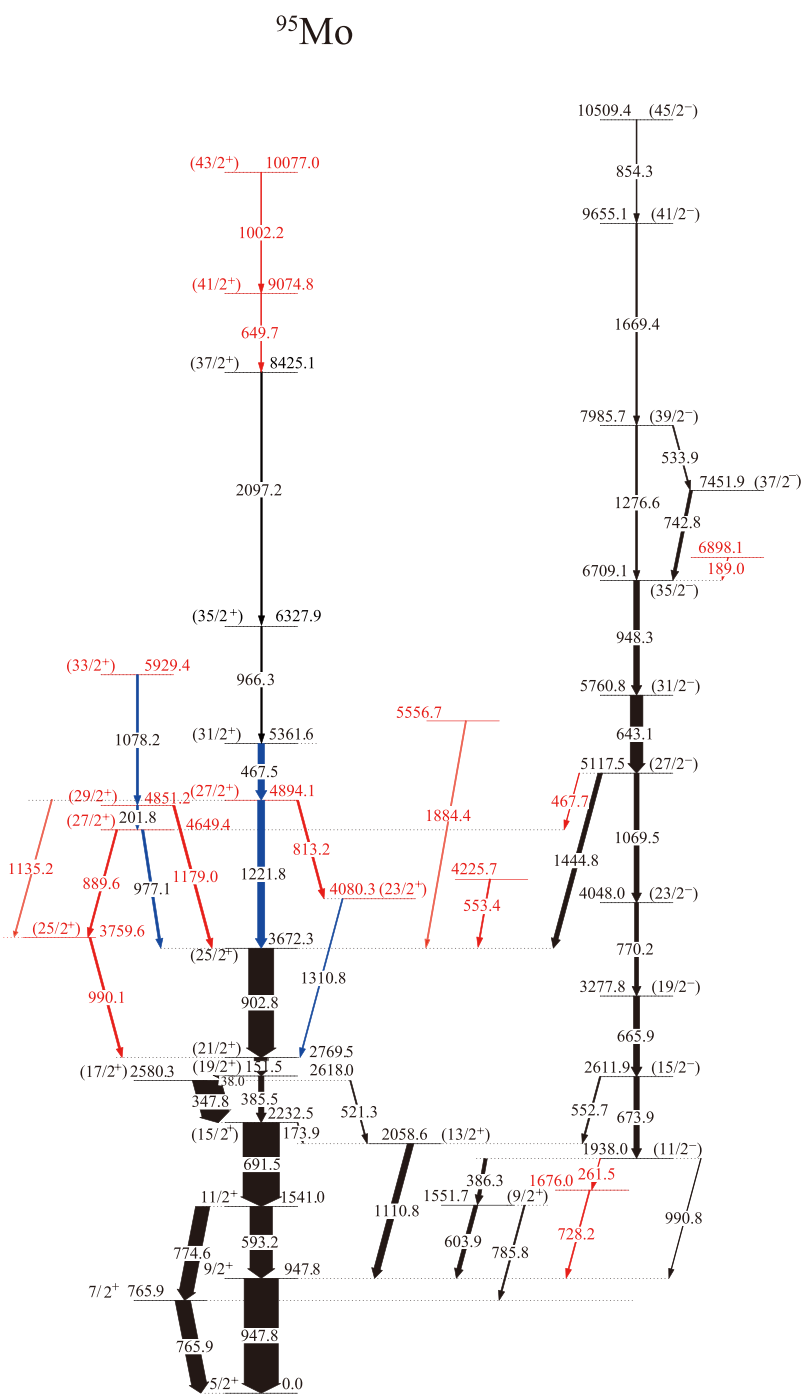

Fig. 1. (color online) Level scheme of ^{95}Mo established in the present study. The thicknesses of the arrows are approximately proportional to the γ-ray intensity listed in Table 1. The new and rearranged γ rays are marked in red and blue, respectively.

ratios from the present data, previously reported data, and shell-model calculations, are also presented in Table 1. Gated coincidence spectra from the E_γ-E_γ matrix, constructed based on the present experimental results, are displayed in Figs. 3(a)(b). In addition, double-gated coincidence spectra from the E_γ-E_γ-E_γ cube are displayed in Figs. 4(a)-(d) and 5(a)(b). The double-coincidence gated spectra in Figs. 3(a)(b) and triple-coincidence gated spectra in Figs. 4(a) and 5(b) show all the new transitions as well as the previously reported ones. Key details are discussed as follows.

As shown in Fig. 4(b), new transitions at 649.7 and 1002.2 keV are observed in the double-gated coincidence spectra of the 467.5-, 691.5-keV and the 467.5-, 347.8-keV γ-ray transitions. Further gating analysis confirms that the 649.7- and 1002.2-keV transitions are in mutual

Table 1. γ-ray transition energies, relative intensities, ADO ratios, and their assignments in ^{95}Mo.

E_γ/keV	I_γ	$R_{\rm ADO}$	E_i/keV	E_f/keV	J_i^π	J_f^π	multipolarity
38.0	-	-	2618.0	2580.3	$(19/2^+)$	$(17/2^+)$	$(M1/E2)$
151.5(1)	36.0(7)	1.06(9)	2769.5	2618.0	$(21/2^+)$	$(19/2^+)$	$(M1/E2)$
173.9(11)	4.3(4)	0.92(10)	2232.5	2058.6	$(15/2^+)$	$(13/2^+)$	$(M1/E2)$
189.0(10)*	1.7(8)	-	6898.1	6709.1	-	$(35/2^-)$	-
201.8(5)	5.6(7)	1.04(3)	4851.2	4649.4	$(29/2^+)$	$(27/2^+)$	$(M1/E2)$
261.5(3)*	1.8(8)	-	1938.0	1676.0	$(11/2^-)$	-	-
347.8(1)	75.6(6)	1.07(2)	2580.3	2232.5	$(17/2^+)$	$(15/2^+)$	$(M1/E2)$
385.5(3)	14.8(13)	1.54(2)	2618.0	2232.5	$(19/2^+)$	(15/2+)	$(E2)$
386.3(3)	9.4(5)	1.10(4)	1938.0	1551.7	$(11/2^-)$	$(9/2^+)$	$(E1)$
467.5(1)	17.7(10)	1.66(2)	5361.6	4894.1	$(31/2^+)$	$(27/1^+)$	$(E2)$
467.7(2)*	1.9(2)	-	4894.1	4649.4	$(27/2^-)$	$(27/2^+)$	$(E1)$
521.3(5)	3.6(5)	1.58(3)	2618.0	2058.6	$(17/2^+)$	$(13/2^+)$	$(E2)$
553.9(4)	3.5(2)	0.87(2)	7985.7	7451.9	$(39/2^-)$	$(37/2^-)$	$(M1/E2)$
552.7(2)	4.2(4)	0.99(3)	2611.9	2058.6	$(15/2^-)$	$(13/2^+)$	$(E1)$
553.4(6)*	2.0(7)	-	4225.7	3672.3	-	$(25/2^+)$	-
593.2(1)	61.7(2)	0.92(1)	1541.0	947.8	$11/2^+$	$9/2^+$	$M1/E2$
603.9(2)	11.3(2)	1.68(3)	1551.7	947.8	$(9/2^+)$	$9/2^+$	$(M1/E2)$
643.1(2)	34.8(13)	1.41(1)	5760.8	5117.5	$(31/2^-)$	$(27/2^-)$	$(E2)$
649.7(2)*	2.3(3)	1.30(12)	9074.8	8425.1	$(41/2^+)$	$(37/2^+)$	$(E2)$
665.9(1)	16.9(4)	1.36(2)	3277.8	2611.9	$(19/2^-)$	$15/2^-$	$(E2)$
673.9(1)	14.6(3)	1.71(2)	2611.9	1938.0	$(15/2^-)$	$(11/2^-)$	$(E2)$
691.5(1)	100(1)	1.39(1)	2232.5	1541.0	$(15/2^+)$	$11/2^+$	$(E2)$
728.2(10)*	1.9(1)	-	1676.0	947.8	-	$9/2^+$	-
742.8(7)	8.5(4)	0.90(3)	7451.9	6709.1	$(37/2^-)$	$(35/2^-)$	$(M1/E2)$
765.9(1)	41.8(2)	1.09(1)	765.9	0	$7/2^+$	$5/2^+$	$M1/E2$
770.2(1)	11.2(7)	1.43(2)	4048.0	3277.8	$(23/2^-)$	$(19/2^-)$	$(E2)$
774.6(1)	38.6(7)	1.36(2)	1541.0	765.9	$11/2^+$	$7/2^+$	$E2$
785.8(6)	4.2(10)	0.80(3)	1551.7	947.8	$(9/2^+)$	$7/2^+$	$(M1/E2)$
813.2(6)*	3.2(2)	1.42(6)	4894.1	4080.3	$(27/2^+)$	$(23/2^+)$	$(E2)$
854.3(9)	2.5(3)	1.23(6)	10509.4	9655.1	$(45/2^-)$	$(41/2^-)$	$(E2)$
889.6(2)*	4.9(5)	0.76(3)	4649.4	3759.6	$(25/2^+)$	$(21/2^+)$	$(E2)$
902.8(2)	69.0(2)	1.35(1)	3672.3	2769.5	$(25/2^+)$	$(21/2^+)$	$(E2)$
947.8(1)	93.9(2)	1.29(1)	947.8	0	$9/2^+$	$5/2^+$	$E2$
948.3(2)	15.5(6)	1.54(2)	6709.1	5760.8	$(35/2^-)$	$(31/2^-)$	$(E2)$
966.3(4)	3.9(4)	1.59(5)	6327.9	5361.6	$(35/2^+)$	$(31/2^+)$	$(E2)$
977.1(2)	9.8(3)	0.98(2)	4649.4	3672.3	$(27/2^+)$	$(25/2^+)$	$(M1/E2)$
990.1(3)*	5.9(5)	1.30(3)	3759.6	2769.5	$(25/2^+)$	$(21/2^+)$	$(E2)$
990.8(7)	1.8(3)	-	1938.0	947.8	$(11/2^-)$	$9/2^+$	$(E1)$
1002.2(3)*	2.3(3)	0.97(5)	10077.0	9074.8	$(43/2^+)$	$(41/2^+)$	$(M1/E2)$
1069.5(4)*	13.7(1)	1.87(5)	5117.5	4048.0	$(27/2^-)$	$(23/2^-)$	$(E2)$
1078.2(2)	6.1(5)	1.33(10)	5929.4	4851.2	$(33/2^+)$	$(29/2^+)$	$(E2)$

Continued on next page

Table 1-continued from previous page

E_γ/keV	I_γ	$R_{\rm ADO}$	E_i/keV	E_f/keV	J_i^π	J_f^π	multipolarity
1110.8(3)	17.4(1)	1.33(2)	2058.6	947.8	$(13/2^+)$	$9/2^+$	$(E2)$
1135.2(4)*	3.5(6)	0.93(10)	4894.1	3759.6	$(27/2^+)$	$(25/2^+)$	$(M1/E2)$
1179.0(3)*	6.3(6)	1.41(6)	4851.2	3672.3	$(29/2^+)$	$(25/2^+)$	$(E2)$
1221.8(2)*	19.3(1)	1.05(2)	4894.1	3672.3	$(27/2^+)$	$(25/2^+)$	$(M1/E2)$
1276.6(2)*	5.2(5)	1.53(5)	7985.7	6709.1	$(39/2^-)$	$(35/2^-)$	$(E2)$
1310.8(3)	3.3(4)	0.87(2)	4080.3	2769.5	$(23/2^+)$	$(21/2^+)$	$(M1/E2)$
1444.8(2)	12.5(1)	1.09(2)	5117.5	3672.3	$(27/2^-)$	$(25/2^+)$	$(E1)$
1669.4(4)	4.0(5)	0.81(3)	9655.1	7985.7	$(41/2^-)$	$(39/2^-)$	$(M1/E2)$
1884.4(6)*	1.5(6)	-	5556.7	3672.3	-	$(25/2^+)$	-
2097.2(6)	4.0(6)	0.68(2)	8425.1	6327.9	$(37/2^+)$	$(35/2^+)$	$(M1/E2)$

[a]The asterisks denote newly identified γ -ray transitions.

[b]Intensities of transitions are normalized to the 691.5 keV γ ray.

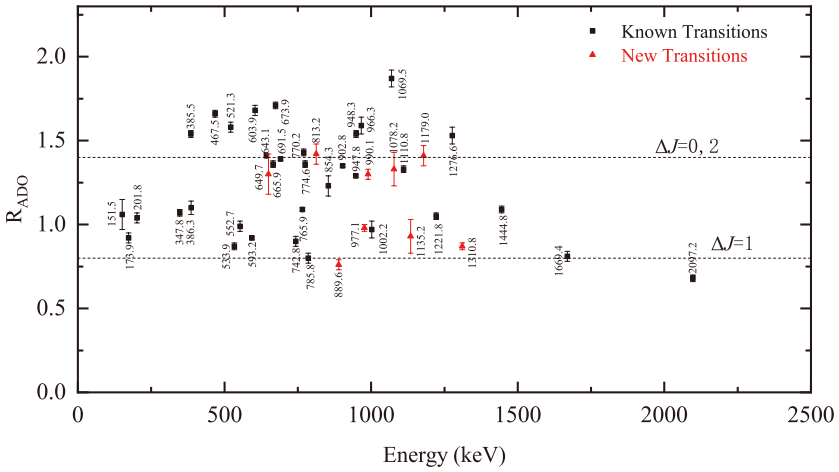

Fig. 2. (color online) $R_{\rm ADO}$ plotted for the γ-ray transitions of ^{95}Mo. The lines correspond to the value of $R_{\rm ADO}$ for the known quadrupoles and dipoles. The quoted error includes the error due to background subtraction, fitting, and efficiency correction.

coincidence and also coincide with the connecting transitions, including and below the 966.3- and 2097.2-keV transitions. Thus, these two transitions are tentatively positioned above the 2097.2-keV transition. Based on the ADO ratio information, the level at 9074.8 keV, which is deexcited by the 649.7-keV transition, is tentatively assigned a spin-parity of $41/2^+$. Similarly, the level at 10077.0 keV, deexcited by the 1002.2-keV transition, is tentatively assigned a spin-parity of $43/2^+$.

As shown in Fig. 1, in the present study, the 467.5- and 1221.8-keV transitions are repositioned, and the new 813.2- and 1310.8-keV transitions are positioned parallel to the 1221.8- and 902.8-keV transitions. The rationale for these adjustments is illustrated in Figs. 4(b) and (c). In Fig. 4(b), the 813.2 keV and 1310.8 keV transitions are distinctly visible in the summed spectrum of the double gates on the 467.5-, 691.5-keV transitions and 467.5-, 347.8-keV transitions; the 902.8 keV and 1221.8 keV transitions are also observed. Conversely, the double-gated spectrum of the 902.8- and 347.8-keV γ rays, shown in Fig. 4(c), reveals the 1221.8-keV transition; however, no evidence of the 813.2- and 1310.8-keV γ transitions is obtained. Further coincidence analysis confirms that the 813.2- and 1310.8-keV transitions are in mutual coincidence. This result indicates that the 813.2- and 1310.8-keV transitions do not coincide with the 902.8- and 1221.8-keV transitions. Furthermore, the sum of the energies of the 813.2- and 1310.8-keV transitions is approximately equal to that of the energies of the 902.8- and 1221.8-keV transitions. All these transitions share coincidence relationships with the 467.5-keV transition. Based on this evidence, the placements of the 467.5- and 1221.8-keV transitions are interchanged. The level at 4894.1 keV, associated with the 1221.8-keV transition, is tentatively assigned a spin-parity of $27/2^+$ based on the ADO ratio of transition. Based on the ADO ratios listed in Table 1 for the 813.2- and 1310.8-keV transitions, their multipolarities are assigned as quadru-

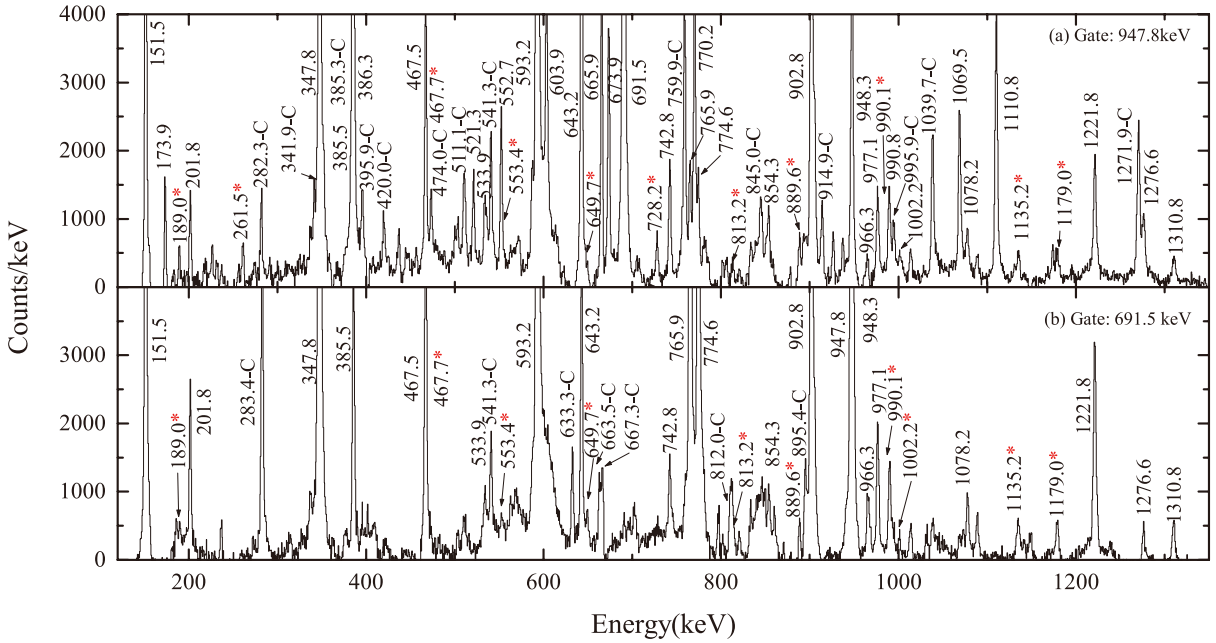

Fig. 3. (color online) Typical gated γ-ray coincidence spectrum at 947.8 keV (a) and gated γ-ray coincidence spectrum at 691.5 keV (b). The contaminant peaks are labeled as C, indicating that they originate from other nuclei.

pole and dipole, respectively. Consequently, the spin-parity of the level at 4080.3 keV is assigned as $(23/2^+)$. Notably, as shown in Figs. 4(a) and (c), the 553.4- and 1884.4-keV transitions are tentatively placed above the level at 3672.3 keV, based on the available coincidence relationships.

Based on the observed coincidence relationships, the presence of the 201.8-keV transition, along with its coincident partners at 977.1 and 1078.2 keV, is confirmed. In conjunction with the newly identified transitions at 889.6, 990.1, and 1179.0 keV and guided by their mutual coincidence relationships, their placements within the level scheme are revised as depicted in Fig. 1. As shown in Fig. 4(d), the new transitions at 889.6, 990.1, 977.1, and 1078.2 keV appear in the summed spectrum of the double gates on the 201.8-keV transition with the 347.8-keV and 691.5-keV transitions. Further coincidence analysis confirms that the 977.1- and 1078.2-keV transitions are mutually coincident. Moreover, these transitions, including the 201.8-keV transition, exhibit coincidence relationships with the 902.8-keV transition and the deexciting levels below it (Figs. 4(a) and (c)). Consequently, these three transitions are placed above the 902.8-keV transition. As shown in Fig. 4(c), the new 1179.0-keV transition is in coincidence with the 1078.2-keV transition as well as with the 902.8-keV transition and those below it. However, it shows no coincidence with the 201.8-keV transition, as confirmed by its absence in Fig. 4(d). Furthermore, the 1179.0-keV transition is not coincident with the 977.1-keV transition. Given that the sum of the energies of the 201.8- and 977.1-keV transitions well aligns with the energy of the 1179.0-keV transition, the 1179.0-keV transition is placed parallel to the 201.8- and 977.1-keV transitions, thereby deexciting the level at 3672.3 keV. Additionally, the 889.6- and 990.1-keV transitions are mutually coincident. Fig. 4(d) also indicates that they are not coincident with the 902.8-keV transition. The sum of their energies well aligns with that of the energies of the 977.1- and 902.8-keV transitions. Therefore, the 889.6- and 990.1-keV transitions are placed above the level at 2769.5 keV and connected via the 201.8-keV transition. Based on the ADO ratio information, the level at 4649.4 keV, which is deexcited by both the 977.1- and 889.6-keV transitions, is tentatively assigned a spin-parity of $27/2^+$. The level at 3759.6 keV, deexcited by the 990.1-keV transition, is tentatively assigned a spin-parity of $25/2^+$. The spin-parities of the levels at 4851.2 keV and 5929.4 keV are tentatively assigned as $29/2^+$ and $33/2^+$, respectively. Notably, as shown in Fig. 4(b), the 1135.2-keV transition is in coincidence with the 467.5-keV transition. Further coincidence analysis reveals that the 1135.2-keV transition also coincides with the 990.1-keV transition as well as with the connecting transitions below it. Moreover, the sum of the energies of the 1135.2- and 990.1-keV transitions is approximately equal to that of the 1221.8- and 902.8-keV transitions. Therefore, the 1135.2-keV transition is tentatively placed above the 990.1-keV transition, and the level at 4894.1 keV deexcites via the 1135.2-keV transition to that at 3759.6 keV.

As shown in Fig. 5(a) and (b), the 643.1-keV transition is in coincidence with the 467.7-, 889.6-, and 990.1-keV transitions as well as with the 151.5-keV transition and other connecting transitions below it. Furthermore,

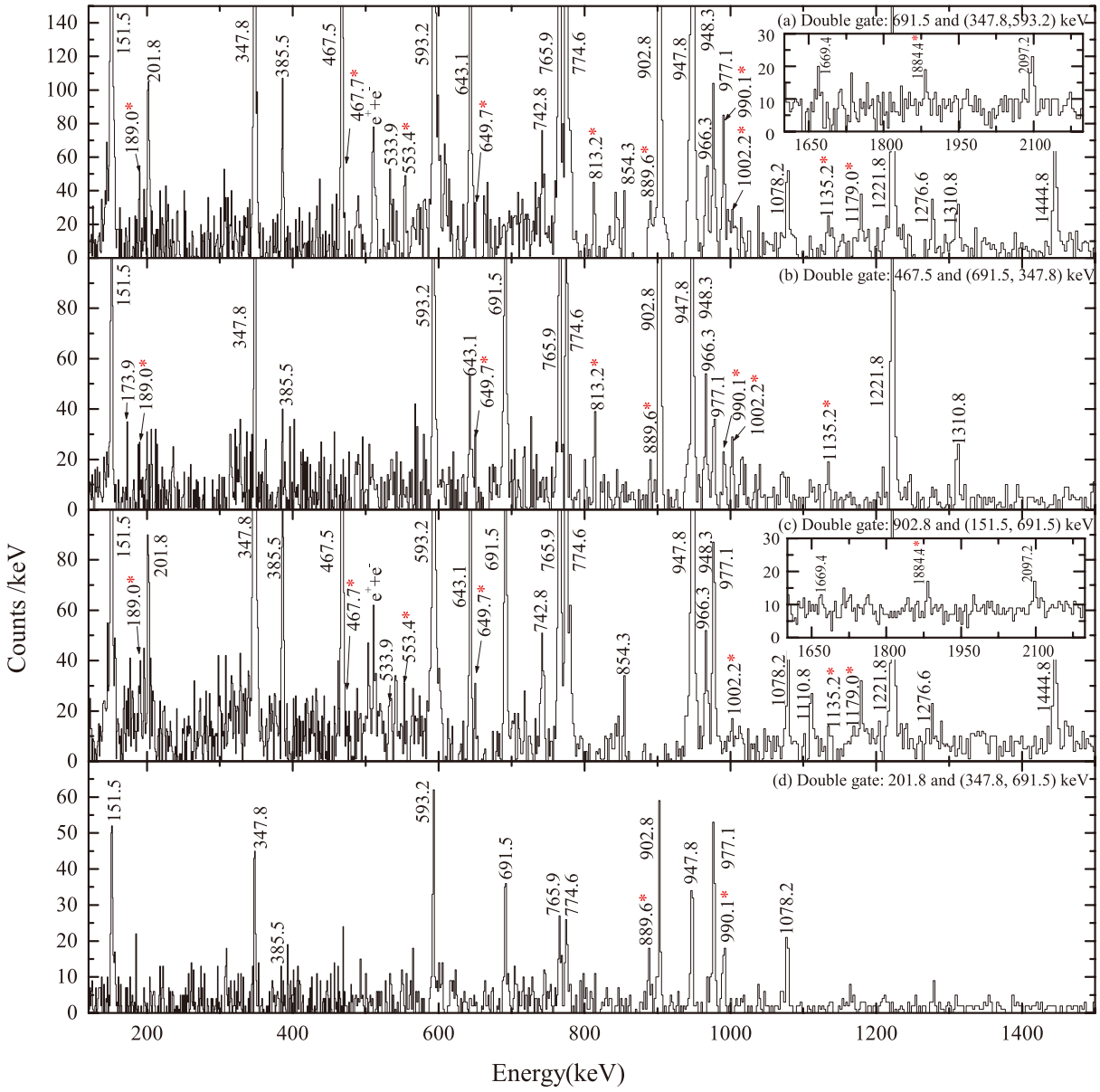

Fig. 4. (color online) Typical double-gated γ-ray coincidence spectra for ^{95}Mo. The spectra are generated by adding spectra selected from the double-gated coincidence spectra with gates on various transition combinations, as labeled.

Fig. 4(b) demonstrates that the 467.7-keV transition is coincident with the 889.6- and 990.1-keV transitions. Consequently, a new 467.7-keV transition, deexciting the level at 5117.5 keV to that at 4649.4 keV, is introduced. Additionally, a new 189.0-keV transition is observed in Fig. 5(a) and (b). Further coincidence analysis indicates that the 189.0-keV transition tentatively deexcites the level at 6709.1 keV.

As shown in Fig. 5(c), the new transitions at 261.5 and 728.2 keV appear in the double-gated coincidence spectrum of the 947.7- and 673.9-keV transitions. An alternative de-excitation path from the 1938.0-keV level to the $9/2^+$ state, consisting of a cascade of the 261.5- and 728.2-keV transitions, is established. Furthermore, the 1938.0-keV level de-excite via the 261.5-keV transition to the 1676.0-keV level.

IV. DISCUSSIONS

A. Shell-model calculations and systematic studies of neighboring nuclei

To account for the partial level structure observed experimentally in ^{95}Mo, shell-model calculations are performed using the NuShellX code [32]. For a more comprehensive analysis of the level structure of this nucleus, two effective interactions, GWBXG [33] and SNET [34], are employed in the calculations. For the GWBXG inter-

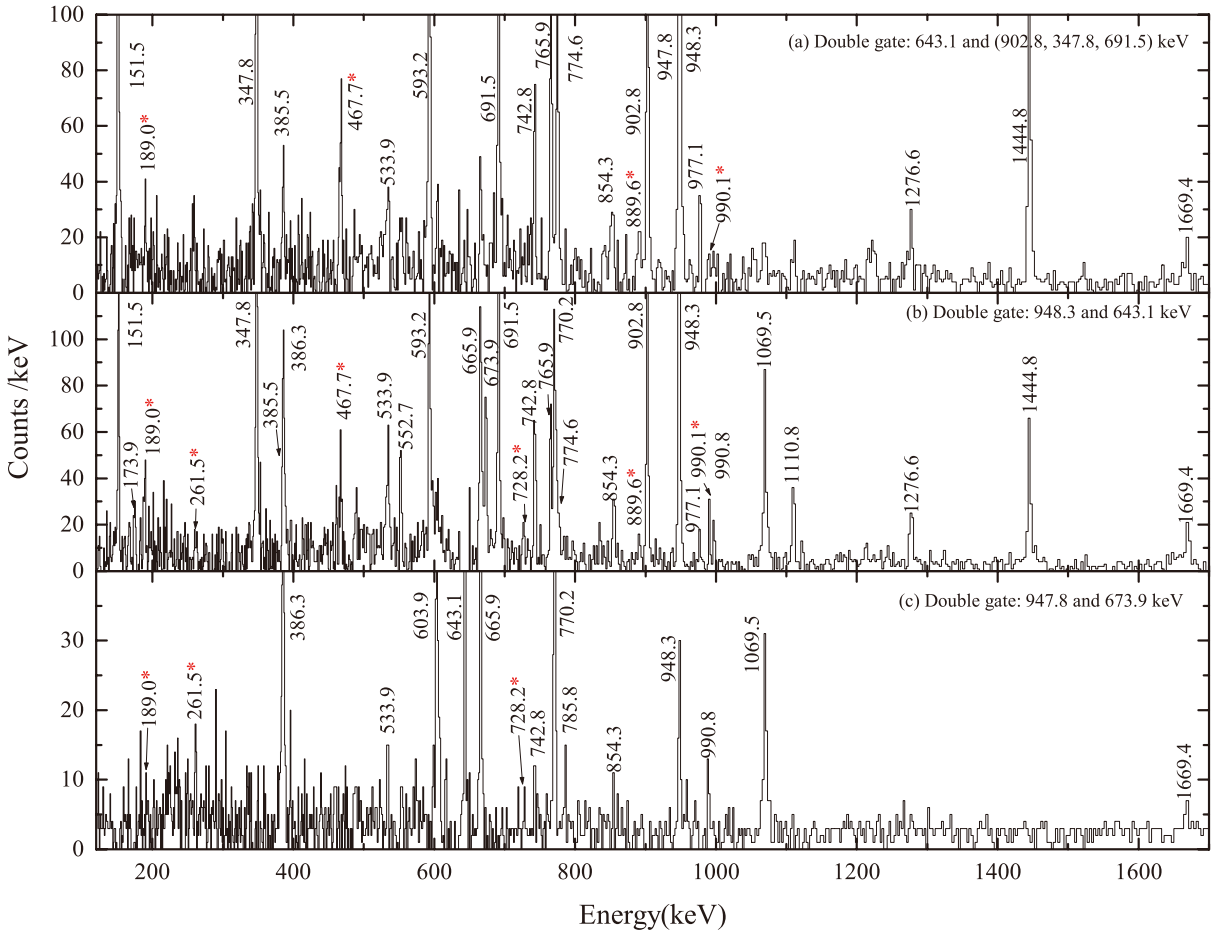

Fig. 5. (color online) Typical double-gated γ-ray coincidence spectra for ^{95}Mo. Figure (a) is generated by summing double-gated coincidence spectra from different transition combinations, as labeled. Figure (b) is the double-gated spectrum on transitions 948.3-keV and 643.1-keV. Figure (c) is the double-gated spectrum on transitions 947.8-keV and 673.9-keV.

action, the model space comprises the four proton orbitals $1f_{5/2}$, $2p_{3/2}$, $2p_{1/2}$, and $1g_{9/2}$ and the six neutron orbitals $2p_{1/2}$, $1g_{9/2}$, $1g_{7/2}$, $2d_{5/2}$, $2d_{3/2}$, and $3s_{1/2}$. The model space for the SNET interaction is larger than that for GWBXG: the proton sector additionally includes the $1g_{7/2}$, $2d_{5/2}$, $2d_{3/2}$, and $3s_{1/2}$ orbitals above the $Z = 50$ closed shell, whereas the neutron sector includes the $1f_{5/2}$, $2p_{1/2}$ orbitals above the $N = 28$ closed shell and the $1h_{11/2}$ orbital above the $N = 50$ closed shell. To obtain reasonable caculation results within accpetable time periods, space truncation is applied in the present calculations. Specifically, for the GWBXG model space, proton excitations are confined within the $1f_{5/2}$, $2p_{3/2}$, $2p_{1/2}$, and $1g_{9/2}$ orbitals, allowing a maximum of two proton excitations from the $1f_{5/2}$ orbital; neutron excitations are restricted to the $1g_{7/2}$, $2d_{5/2}$, $2d_{3/2}$, and $3s_{1/2}$ orbitals above the $N = 50$ core. To facilitate a comparison focusing on the influence of the $1h_{11/2}$ orbital within the SNET interaction, we ensure that the allowed single-particle excitations remain identical to those for the GWBXG interaction, except that one neutron is permitted to occupy the $1h_{11/2}$ orbital. The levels calculatedbased on the two interactions are compared with the experimental data, and the results are shown in Figs. 6 and 7. The calculated energies, their corresponding experimental values, and the resulting configuration information are listed in Tables 2 and 3. As evident from Figs. 6 and 7 and Tables 2 and 3, the results obtained with the GWBXG interaction satisfactorily reproduce most of the lower-lying positive-parity states. In contrast, the SNET interaction generally overestimates the energies of the positive-parity levels; it provides a reasonable description for the low-lying negative-parity states, whereas it underestimates the energies of the higher-lying negative-parity levels. The results of the shell-model calculations are briefly discussed in the following.

For the positive-parity states (Table 2), the two dominant configurations for the ground $5/2^+$ state, calculated with the GWBXG and SNET interactions, are $\pi(g^2_{9/2})\otimes\nu(d^3_{5/2})$ and $\pi(g^4_{9/2})\otimes\nu(d^3_{5/2})$, respectively. As shown in Fig. 6 or Table 2, the calculated energies for the $7/2^+$ state, from both the GWBXG and SNET interactions, deviate from the experimental value by approximately 400 keV. However, the GWBXG interaction suc-

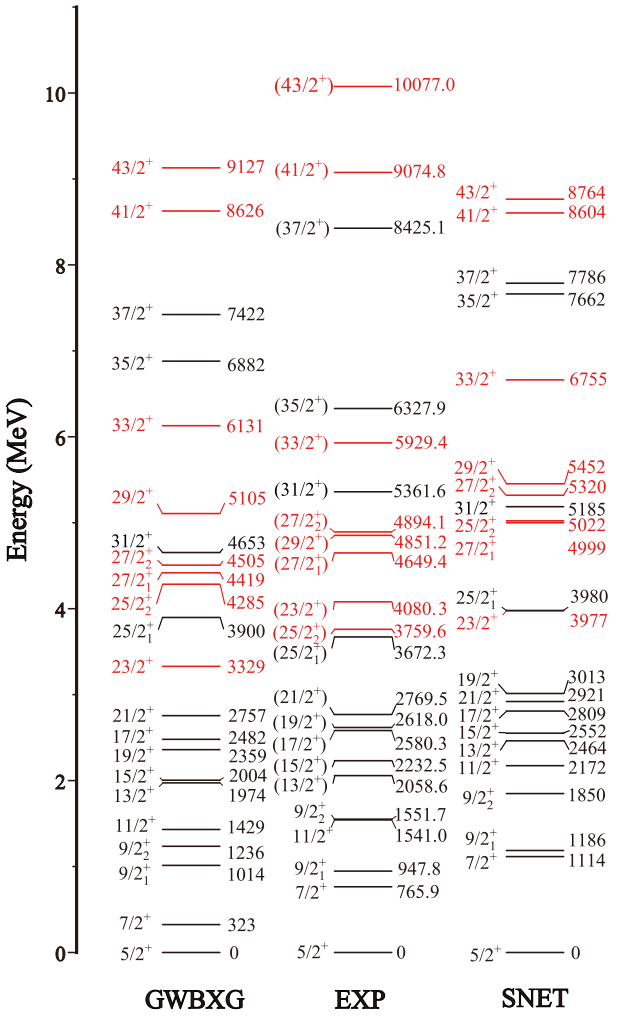

Fig. 6. (color online) Comparison of experimental excitation energies in ^{95}Mo (π=+) with shell-model predictions with GWBXG and SNET interactions.

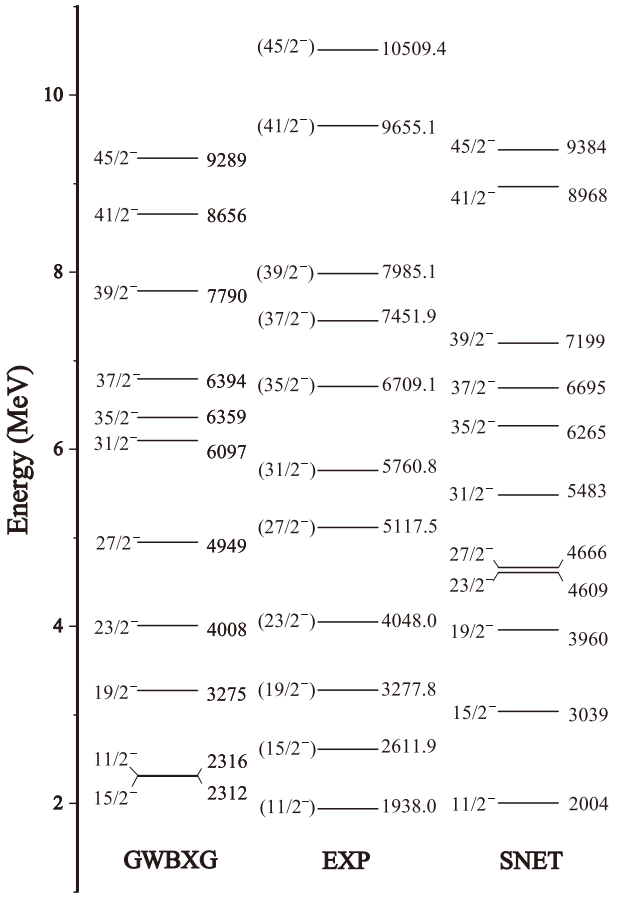

Fig. 7. (color online) Comparison of experimental excitation energies in ^{95}Mo (π=−) with shell-model predictions with GWBXG and SNET interactions.

cessfully reproduces the level order relative to the $9/2^+_1$ state; that is, the position of this state is below the $9/2^+_1$ state. When proton excitations from the $1f_{5/2}$ orbital are fully restricted, the result obtained based on the GWBXG interaction well reproduces the $7/2^+$ state, with a difference of only 120 keV from the experimental value. As listed in Table 2, the configuration components for the $7/2^+$ state are consistent between the two interactions, with the two dominant configurations being $\pi(g^2_{9/2})\otimes\nu(g^1_{7/2}d^2_{5/2})$ and $\pi(g^4_{9/2})\otimes\nu(g^1_{7/2}d^2_{5/2})$. An analysis of the shell-model output reveals that this state originates primarily from the excitation of a neutron from the $2d_{5/2}$ orbital to the $1g_{7/2}$ orbital. In other words, the main angular momentum contribution for this state is $\nu(g^1_{7/2}d^2_{5/2})_{7/2^+}$. For the yrast states from $9/2^+$ to $21/2^+$, the GWBXG interaction well reproduces their experimental energies, with differences of approximately 200 keV, whereas the SNET interaction overestimates the energies of these states. The dominant configuration components for these states are identical for the two interactions. For the $9/2^+_1$ state, the main configuration is $\pi(g^2_{9/2})\otimes\nu(d^3_{5/2})$. This state primarily involves a mixture of the angular momentum contributions $\pi(g^2_{9/2})_{2^+}\otimes\nu(d^3_{5/2})_{5/2^+}$ and $\nu(d^3_{5/2})_{9/2^+}$. The $11/2^+$ and $15/2^+$ states exhibit significant configuration mixing, with the highest-weighted configuration being $\pi(g^2_{9/2})\otimes\nu(g^1_{7/2}d^2_{5/2})$ for both. Within this configuration, the main angular momentum contributions for the $11/2^+$ and $15/2^+$ states are $\nu(g^1_{7/2}d^2_{5/2})_{11/2^+}$ and $\nu(g^1_{7/2}d^2_{5/2})_{15/2^+}$, respectively. The main configuration for both the $13/2^+$ and $17/2^+$ states is $\pi(g^2_{9/2})\otimes\nu(d^3_{5/2})$, and the primary angular momentum contributions for these two states are $\pi(g^2_{9/2})_{4^+}\otimes\nu(d^3_{5/2})_{5/2^+}$ and $\pi(g^2_{9/2})_{6^+}\otimes\nu(d^3_{5/2})_{5/2^+}$, respectively. The main configuration for both the $19/2^+$ and $21/2^+$ states is $\pi(g^2_{9/2})_{8^+}\otimes\nu(d^3_{5/2})_{5/2^+}$. For the $9/2^+_2$ state, the energy yielded by the GWBXG calculation is approximately 300 keV lower than the experimental value, whereas that obtained from the SNET calculation is approximately 300 keV higher than the experimental value. Considering the placement of this state in the level scheme (i.e., the $9/2^+_2$ state de-excites to the $9/2^+_1$ state via a 603.9-keV γ transition), we infer that its dominant

Table 2. Main components of the wave fuctions and their partitions for positive parity states in ^{95}Mo. For $\pi\otimes\nu$, GWBXG represents $\pi(f_{5/2}p_{3/2}p_{1/2}g_{9/2})\otimes\nu(g_{7/2}d_{5/2}d_{3/2}s_{1/2})$. For $\pi\otimes\nu$,SNET represents $\pi(f_{5/2}p_{3/2}p_{1/2}g_{9/2})\otimes\nu(g_{7/2}d_{5/2}d_{3/2}s_{1/2}h_{11/2})$

$I^{\pi}/\hbar$	$E_{\exp}$/keV	$E_{(\mathrm{GWBXG})}$/keV	$E_{(\mathrm{SNET})}$/keV	Wave function $\pi\otimes\nu$(GWBXG)	Partitions (GWBXG)	Wave function $\pi\otimes\nu$(SNET)	Partitions (SNET)
$5/2^+$	0	0	0	6422⊗0300	55.8%	6422⊗ 03000	39.8%
				6404⊗0300	8.4%	6404⊗ 03000	12.0%
$7/2^+$	765.9	323	1114	6422⊗1200	28.5%	6422⊗ 12000	25.1%
				6404⊗1200	18.4%	6404⊗ 12000	16.5%
$9/2^+_1$	947.8	1014	1186	6422⊗0300	51.8%	6422⊗ 03000	48.8%
				6404⊗0300	5.0%	6404⊗ 03000	13.0%
$9/2^+_2$	1551.7	1236	1850	6422⊗1200	22.8%	6422⊗ 03000	45.9%
				6404⊗1200	16.0%	6404⊗ 03000	5.7%
$11/2^+$	1541.0	1429	2172	6422⊗1200	22.1%	6422⊗ 12000	24.2%
				6404⊗1200	17.5%	6404⊗ 12000	14.0%
$13/2^+$	2058.6	1973	2464	6422⊗0300	67.1%	6422⊗ 03000	41.9%
				6422⊗1200	3.23%	6422⊗ 03000	9.8%
$15/2^+$	2232.5	2004	2552	6422⊗1200	29.0%	6422⊗ 12000	38.5%
				6404⊗1200	15.2%	6404⊗ 12000	21.7%
$17/2^+$	2580.3	2482	2809	6422⊗0300	69.9%	6422⊗ 03000	51.2%
				6224⊗0300	4.2%	6404⊗ 03000	7.8%
$19/2^+$	2618.0	2359	3013	6422⊗0300	76.9%	6422⊗ 03000	54.6%
				6224⊗0300	4.5%	6404⊗ 03000	7.4%
$21/2^+$	2769.5	2757	2921	6422⊗0300	70.2%	6422⊗ 03000	50.7%
				6224⊗0300	4.7%	6404⊗ 03000	8.4%
$23/2^+$	4080.3	3329	3977	6422⊗1200	50.0%	6422⊗ 02010	39.8%
				6224⊗1200	12.8%	6422⊗ 03000	19.9%
$25/2^+_1$	3672.3	3900	3980	6422⊗0300	70.1%	6422⊗ 03000	64.8%
				6422⊗0300	4.9%	6404⊗ 03000	8.7%
$25/2^+_2$	3759.6	4285	5022	6422⊗1200	51.2%	6422⊗ 12000	45.6%
				6404⊗1200	8.0%	6404⊗ 12000	17.1%
$27/2^+_1$	4649.4	4419	4999	6422⊗1200	25.8%	6422⊗ 12000	45.1%
				6404⊗1200	20.0%	6404⊗ 12000	12.9%
$27/2^+_2$	4894.1	4505	5320	6422⊗1200	38.2%	6422⊗ 12000	45.5%
				6404⊗1200	15.5%	6404⊗ 12000	23.9%
$29/2^+$	4851.2	5105	5452	6422⊗1200	34.7%	6422⊗ 12000	56.2%
				6404⊗1200	17.2%	6404⊗ 12000	17.1%
$31/2^+$	5361.6	4653	5185	6422⊗1200	73.6%	6422⊗ 12000	66.2%
				6404⊗1200	8.1%	6404⊗ 12000	17.4%
$33/2^+$	5929.4	6131	6664	6422⊗2100	31.1%	6404⊗ 21000	37.4%
				6404⊗2100	28.0%	6422⊗ 21000	36.6%
$35/2^+$	6327.9	6882	7662	6404⊗1200	22.0%	6404⊗ 12000	54.0%
				5414⊗1200	20.7%	4424⊗ 12000	9.7%
$37/2^+$	8425.1	7422	7786	5414⊗1200	54.9	6413⊗ 02001	74.6%
				5324⊗1200	9.4%	6323⊗ 02001	5.8%

Continued on next page

Table 2-continued from previous page

$I^{\pi}/\hbar$	$E_{\rm exp}$/keV	$E_{\rm (GWBXG)}$/keV	$E_{\rm (SNET)}$/keV	Wave function $\pi\otimes\nu$(GWBXG)	Partitions (GWBXG)	Wave function $\pi\otimes\nu$(SNET)	Partitions (SNET)
$41/2^+$	9074.8	8626	8604	6404⊗2100	34.2%	6413⊗ 02001	57.2%
				6314⊗2100	13.2%	6413⊗ 11001	10.4%
$43/2^+$	10077.0	9127	8764	5414⊗1200	59.6%	6422⊗11010	86.0%
				5324⊗1200	23.1%	6323⊗11001	3.9%

Table 3. Similar to Table 2, but for the negative parity states.

$I^{\pi}/\hbar$	$E_{\rm exp}$/keV	$E_{\rm (GWBXG)}$/keV	$E_{\rm (SNET)}$/keV	Wave function $\pi\otimes\nu$(GWBXG)	Partitions (GWBXG)	Wave function $\pi\otimes\nu$(SNET)	Partitions (SNET)
$11/2^-$	1938.0	2316	2004	6413⊗ 0300	49.1%	6422⊗ 02001	32.3%
				5423⊗ 0300	11.6%	6404⊗02001	14.4%
$15/2^-$	2611.9	2312	3039	6413⊗ 1200	54.8%	6422⊗ 02001	46.2%
				5423⊗ 1200	12.3%	6404⊗02001	17.4%
$19/2^-$	3277.8	3275	3960	6413⊗ 1200	31.2%	6422⊗ 02001	27.9%
				5423⊗ 1200	26.5%	6404⊗02001	12.1%
$23/2^-$	4048.0	4008	4609	6413⊗ 1200	48.9%	6422⊗ 02001	30.3%
				5423⊗ 1200	19.0%	6404⊗02001	8.3%
$27/2^-$	5117.5	4949	4666	6413⊗ 1200	39.4%	6422⊗ 02001	44.7%
				6323⊗ 1200	22.2%	6404⊗02001	11.4%
$31/2^-$	5760.8	6097	5483	6413⊗ 1200	58.2%	6422⊗ 02001	66.4%
				6323⊗ 1200	8.7%	6404⊗02001	12.5%
$35/2^-$	6709.1	6359	6265	6413⊗ 1200	58.6%	6422⊗ 02001	59.4%
				6323⊗ 1200	25.4%	6404⊗02001	10.7%
$37/2^-$	7451.9	6794	6695	6413⊗ 1200	84.1%	6422⊗ 11001	56.9%
				6323⊗ 1200	3.5%	6404⊗11001	25.1%
$39/2^-$	7985.1	7790	7199	6413⊗ 2100	86.6%	6422⊗ 11001	53.8%
				6215⊗ 2100	3.4%	6404⊗11001	24.2%
$41/2^-$	9655.1	8656	8968	5423⊗ 1200	64.2%	6404⊗ 11001	65.6%
				5405⊗ 1200	15.1%	6314⊗11001	6.3%
$43/2^-$	10509.4	9289	9384	5405⊗ 2100	48.0%	6404⊗ 11001	46.4%
				5423⊗ 2100	15.5%	6314⊗11001	7.0%

configuration likely differs from that of the $9/2^+_1$ state and is $\pi(g^2_{9/2})\otimes\nu(g^1_{7/2}d^2_{5/2})$. The main angular momentum contribution for this state is also a mixture of $\pi(g^2_{9/2})_{2^+}\otimes\nu(g^1_{7/1}d^2_{5/2})_{7/2^+}$ and $\nu(d^3_{5/2})_{9/2^+}$. For the newly identified $23/2^+$ state, the SNET interaction well reproduces its energy, whereas the GWBXG interaction underestimates it. The dominant configurations obtained from the two interactions differ: the SNET result yields $\pi(g^2_{9/2})\otimes\nu(d^2_{5/2}s^1_{1/2})$, whereas the GWBXG result gives $\pi(g^2_{9/2})\otimes\nu(g^1_{7/2}d^2_{5/2})$. For the $25/2^+_1$ state, the results from both the GWBXG and SNET interactions differ from the experimental value by approximately 300 keV, and both calculations yield the same dominant configuration $\pi(g^2_{9/2})\otimes\nu(d^3_{5/2})$. For the newly identified $25/2^+_1$ state, the results obtained from both the interaction calculations show significant deviations from the experimental value. For the two newly identified $27/2^+$ state and the $29/2^+$ state, the GWBXG calculations well reproduce their experimental energies, whereas the SNET results generally exceed the experimental values; the dominant configuration for these three states is $\pi(g^2_{9/2})\otimes\nu(g^1_{7/2}d^2_{5/2})$. For the $31/2^+$ state and higher, the GWBXG and SNET interaction calculations cannot reproduce the experimental values, with deviations reaching 600 keV.

For the negative-parity states (Fig. 7 and Table 3), the energy of the $11/2^-$ state, calculated with the SNET inter-

action, agrees well with the experimental value, deviating by only 66 keV. In contrast, the result obtained with the GWBXG interaction shows a significant discrepancy for this level. This deviation is observed likely because the GWBXG interaction does not include the $h_{11/2}$ orbital, and thus, the dominant configuration is markedly different from that obtained from the SNET calculation. The dominant configuration for the $11/2^-$ state, obtained with the SNET interaction, is $\pi(g^2_{9/2})_{0^+}\otimes\nu(d^2_{5/2}h^1_{11/2})_{11/2^-}$. Notably, an earlier ^{94}Mo$(d,p)^{95}$Mo knockout reaction experiment, reported in Ref. [35], in which the angular distribution of the proton spectrum is analyzed, reveals that the single-particle $h_{11/2}$ strength dominates the 1930-keV level, indicating a substantial $h_{11/2}$ configuration component in this state. Therefore, the SNET calculation provides a satisfactory description of the $11/2^-$ state. Furthermore, as mentioned in Sec. I, systematic observations in the neighboring odd-A nuclei of ^{95}Mo with increasing neutron number reveal similar $11/2^-$ states, followed by $\Delta I = 2$ rotational-like bands built upon these states [10–16, 36]. For instance, a rotational-like band developed on the $11/2^-$ state in ^{97}Ru [13] has been interpreted as a decoupled band based on an $h_{11/2}$ quasineutron configuration. Similarly, neutron $h_{11/2}$ decoupled bands have been observed in ^{97,99,101}Mo [12]. As illustrated in Fig. 1, a similar rotational-like band appears above the $11/2^-$ state in ^{95}Mo. This observation suggests that collectivity may emerge above the $11/2^-$ state. This could explain why the SNET interaction fails to satisfactorily reproduce the energies of the $15/2^-$ state and those higher.

To further understand the structure of ^{95}Mo, a systematic comparison of the yrast positive-parity low-lying excited states among the $N = 53$ isotones ^{95}Mo, ^{97}Ru, and ^{99}Pd is presented in Fig. 8. Notably, the GWBXG and SNET interactions are also employed to calculate the level structures of ^{97}Ru and ^{99}Pd using the same model space truncation scheme as that applied for ^{95}Mo. The results indicate that the dominant configurations for the corresponding states in ^{97}Ru and ^{99}Pd, obtained from the two interactions, are neither identical to each other nor fully consistent with those of ^{95}Mo. The primary discrepancy lies in the competition between the $\nu(d^3_{5/2})$ and $\nu(g^1_{7/2}d^2_{5/2})$ configurations. However, for the $7/2^+$, $11/2^+$, and $15/2^+$ yrast states in all the three nuclei, the shell-model results obtained from both the interactions consistently yield the configuration $\pi(g^n_{9/2})\otimes\nu(g^1_{7/2}d^2_{5/2})$ (where n denotes the number of valence protons relative to the $Z = 40$ closed shell). This result indicates that these states show identical neutron configurations, namely, $\nu(g^1_{7/2}d^2_{5/2})$. Indeed, the identity of the neutron configurations across these states is naturally expected according to the rules of angular momentum coupling. From Fig. 8, it is observed that the energy of the $7/2^+$ state systematically decreases with increasing proton number. As discussed previously, the $7/2^+$ state arises primarily from a neutron excitation from the $2d_{5/2}$ orbital to the $1g_{7/2}$ orbital. The observed decrease in its energy with increasing proton number may be attributed to a reduction in the energy gap between the $\nu 1g_{7/2}$ and $\nu 2d_{5/2}$ orbitals; this energy gap reduction is potentially caused by the enhanced interaction between the $\nu 1g_{7/2}$ and $\pi 1g_{9/2}$ orbitals due to proton addition. Furthermore, Fig. 8 reveals that the magnitudes of the energy reduction for the $11/2^+$ and $15/2^+$ states with increasing proton number are similar to that of energy of the $7/2^+$ state. The $11/2^+$ and $15/2^+$ states originate from the coupling of a $\nu g_{7/2}$ neutron to the 2^+ and 4^+ states of the adjacent even-even core nuclei, respectively. Notably, the 2^+_1 and 4^+_1 level energies of the adjacent even-even core nuclei — ^{94}Mo [9], ^{96}Ru [13], and ^{98}Pd [38] —are similar; that is, the energy of the $\nu g_{7/2}$ single-particle orbital likely decreases progressively with proton addition.

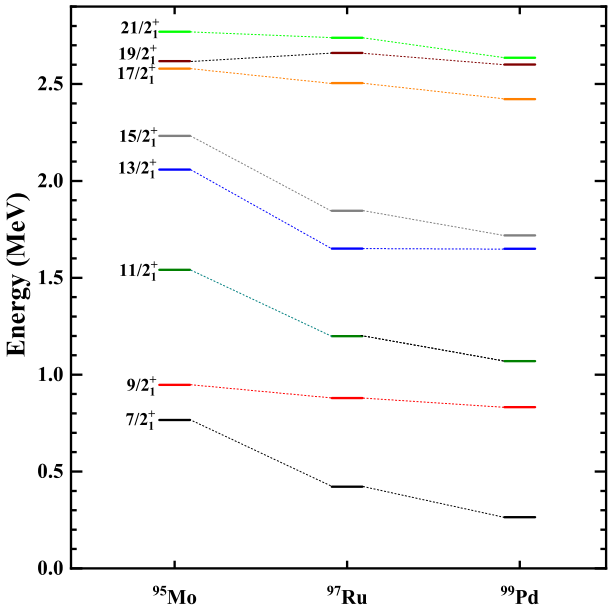

Fig. 8. (color online) Systematics of selected energy levels in ^{95}Mo, ^{97}Ru[13], and ^{99}Pd[37].

As discussed earlier, the $9/2^+$, $13/2^+$, $17/2^+$, and $19/2^+$ states in ^{95}Mo, as calculated by the shell model, are primarily formed by coupling $\nu(d^3_{5/2})_{5/2^+}$ with the $g^2_{9/2}$ proton pairs having angular momenta of 2^+, 4^+, 6^+, and 8^+, respectively. Notably, for a system with a semi-magic neutron core, the 2^+, 4^+, 6^+, and 8^+ states, formed by two protons in the $g_{9/2}$ orbital, follow a seniority scheme [1, 7, 39]. For ^{95}Mo, ^{97}Ru, and ^{99}Pd, which have three valence neutrons, a seniority scheme is not realized. However, the underlying structure may still involve seniority conservation. For instance, the $21/2^+$ state in ^{97}Ru is an isomeric state with a lifetime of 7.8 ns [40], likely due to its significant $(g^4_{9/2})_{8^+}$ proton configuration component.

Shell-model calculations using the GWBXG interaction confirm such a configuration for the $21/2^+$ state, whereas the $19/2^+$ state exhibits a dominant $(g^4_{9/2})_{6^+}$ proton configuration. Similar results are obtained for ^{99}Pd. In contrast, for ^{95}Mo, as mentioned before, the shell-model calculations indicate that the dominant proton configurations for the $19/2^+$ and $17/2^+$ states are $(g^2_{9/2})_{8^+}$ and $(g^2_{9/2})_{6^+}$, respectively. As shown in Fig. 8, the energy spacings among the $17/2^+$, $19/2^+$, and $21/2^+$ states in ^{97}Ru and ^{99}Pd exhibit similar evolution patterns, i.e., relatively small energy gaps are observed between the $19/2^+$ and $21/2^+$ states, differing from the pattern observed in ^{95}Mo. Notably, the dominant neutron configuration of the $19/2^+$ state in ^{95}Mo is $\nu(d^3_{5/2})$, which differs from the $\nu(g^1_{7/2}d^2_{5/2})$ configuration calculated for ^{97}Ru and ^{99}Pd using the GWBXG interaction.

B. 3DTAC-CDFT calculations

As mentioned in Sec. IV.A, the level structure built upon the $11/2^-$ state in ^{95}Mo resembles the decoupled bands systematically observed in neighboring nuclei such as ^{97,99,101}Mo [12] and ^{97}Ru [13, 36]. This result suggests that collectivity, similar to that in neighboring odd-A nuclei, may also emerge in ^{95}Mo. In the present study, the nucleus ^{95}Mo is investigated using the 3DTAC-CDFT with the point-coupling interaction PC-PK1. The 3DTAC-CDFT is a fully microscopic and self-consistent method for describing nuclear rotational structures without introducing additional parameters. It has been successfully applied to the study of various rotational phenomena in nuclei, including magnetic rotation and chiral rotation [41–44]. Details of the numerical calculations are reported in Refs. [42, 45].

Based on the construction of two configurations for the $11/2^-$ state–$\pi(g^2_{9/2})\otimes\nu(d^2_{5/2}h^1_{11/2})$ and $\pi(g^4_{9/2})\otimes\nu(d^2_{5/2}h^1_{11/2})$–the deformation of ^{95}Mo is obtained via 3DTAC-CDFT calculations. As shown in Fig. 9, the calculated quadrupole deformation β and triaxiality γ parameters are $(\beta = 0.14, \gamma = 2.1^\circ)$ and $(\beta = 0.13, \gamma = 5.1^\circ)$, respectively. This result indicates that ^{95}Mo undergoes weakly prolate deformation, suggesting the likely existence of a neutron $h_{11/2}$ decoupled band built on the $11/2^-$ state, similar to those in neighboring nuclei. Furthermore, Kumar *et al.* [12] investigated the aforementioned rotational-like bands (*i.e.*, decoupled bands) in ^{97,99,101}Mo using the cranked shell model, obtaining quadrupole deformation parameters ε_2 ($\varepsilon_2 \approx 0.946\beta$) of 0.19, 0.20, and 0.21, respectively. Combining these results with those obtained in the present study reveals a trend of increasing deformation–and consequently enhanced collectivity–along the Mo isotopic chain with increasing neutron number. In contrast, no rotational-like structure is observed in ^{93}Mo.

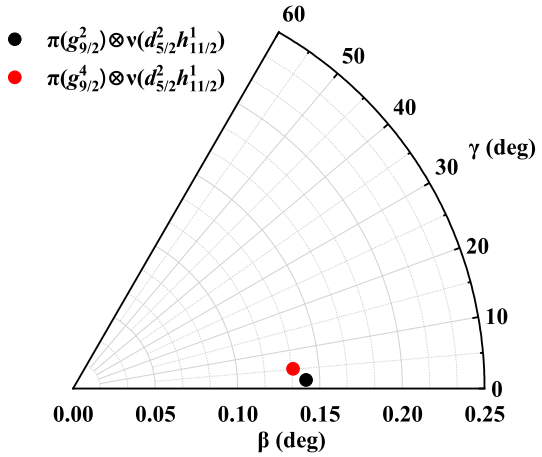

Fig. 9. (color online) Quadrupole and triaxial deformation parameter (β, γ) for ^{95}Mo obtained from 3DTAC-CDFT calculations.

Therefore, ^{95}Mo may represent the critical onset of collectivity in the Mo isotopes.

V. SUMMARY

Excited states in ^{95}Mo were populated via the ^{12}C+^{87}Rb fusion-evaporation reaction at a beam energy of 62 MeV. Based on coincidence analysis, the level scheme of ^{95}Mo was extended and revised: 14 γ-ray transitions and 13 new levels were added, and the placements of 6 transitions were reassigned. Furthermore, several transitions, which were not observed simultaneously in two previous studies, were confirmed, and their positions within the scheme were readjusted. To interpret the observed level structure of ^{95}Mo, shell-model calculations were performed using the GWBXG and SNET effective interactions. The lower-lying positive-parity states were well described by the GWBXG interaction. The calculation with the SNET interaction successfully reproduced a significant $h_{11/2}$ neutron configuration component for the $11/2^-$ state. A systematic analysis of the positive-parity yrast states in the $N = 53$ isotones ^{95}Mo, ^{97}Ru, and ^{99}Pd revealed that the $7/2^+$, $11/2^+$, and $15/2^+$ energies exhibited a nearly identical decreasing trend with increasing proton number. Combined with the shell-model results, we concluded that this phenomenon likely originated from the weakening interaction between the $\nu 1g_{7/2}$ and $\pi 1g_{9/2}$ orbitals with proton addition. Based on the configuration of the $11/2^-$ state, the 3DTAC-CDFT calculations showed that ^{95}Mo. underwent weakly prolate deformation. This result suggests that the level structure built upon the $11/2^-$ state in ^{95}Mo may constitute a neutron $h_{11/2}$ decoupled band, similar to those systematically observed in neighboring nuclei.

References

[1] R. M. Pérez-Vidal, A. Gadea, Domingo-Pardo *et al.*, Phys. Rev. Lett. **129**, 112501 (2022)
[2] S. X. Guan, C. B. Li, Y. Zheng *et al.*, Phys. Rev. C **112**, 014304 (2025)
[3] Y. Hao, Z. Ren, J.-B. Lu *et al.*, Phys. Rev. C **111**, 034312 (2025)
[4] Z. Ren, J.-B. Lu, G.-X. Dong *et al.*, Phys. Rev. C **108**, 044301 (2023)
[5] S. Sihotra, Int. J. Mod. Phys. E **31**, 2250020 (2022)
[6] Y. Q. Li, C. B. Li, Y. Zheng, *et al.*, Phys. Rev. C **110**, 054309 (2024)
[7] Z. Huang, G. X. Zhang, G. L. Zhang *et al.*, Phys. Rev. C **106**, 064331 (2022)
[8] T. Fukuchi, Y. Gono, A. Odahara *et al.*, Eur. Phys. J. A **24**, 249 (2005)
[9] Y. H. Zhang, M. Hasegawa, and W. T. Guo, Phys. Rev. C **79**, 044316 (2009)
[10] D. Bucurescu, G. Căta-Danil, I. Căta-Danil *et al.*, Phys. Rev. C **63**, 014306 (2000)
[11] P. H. Regan, A. D. Yamamoto, F. R. Xu *et al.*, Phys. Rev. C **68**, 044313 (2003)
[12] V. Kumar, R. Chapman, J. Ollier *et al.*, Phys. Rev. C **110**, 044308 (2024)
[13] B. Kharraja, S. S. Ghugre, U. Garg *et al.*, Phys. Rev. C **57**, 83 (1998)
[14] A. D. Yamamoto, P. H. Regan, C. W. Beausang *et al.*, Phys. Rev. C **66**, 024302 (2002)
[15] B. M. Nyakó, J. Gizon, A. Gizon *et al.*, Phys. Rev. C **60**, 024307 (1999)
[16] J. Gizon, D. Jerrestam, A. Gizon *et al.*, Z. Phys. A **345**, 335 (1993)
[17] P. Chauhan, S. Sihotra, R. Joshi *et al.*, Int. J. Mod. Phys. E **33**, 2450042 (2024)
[18] C. Majumder, H. Sharma, S. Tiwary *et al.*, Braz J Phys **49**, 539 (2019)
[19] V. Singh, S. Sihotra, S. Roy *et al.*, J. Phys. G: Nucl. Part. Phys. **44**, 075105 (2017)
[20] T. Numao, H. Nakayama, T. Shibata *et al.*, Nucl. Phys. A **305**, 163 (1978)
[21] R. A. Meyer and R. P. Yaffe, Phys. Rev. C **15**, 390 (1977)
[22] C. Lederer, J. Jaklevic, and J. Hollander, Nucl. Phys. A **169**, 449 (1971)
[23] C. Lederer, J. Jaklevic, and J. Hollander, Nucl. Phys. A **169**, 489 (1971)
[24] L. Mesko, A. Nilsson, S. Hjorth *et al.*, Nucl. Phys. A **181**, 566 (1972)
[25] J. Barrette, M. Barrette, R. Haroutunian *et al.*, Phys. Rev. C **11**, 171 (1975)
[26] P. K. Hopke and R. A. Meyer, Phys. Rev. C **13**, 434 (1976)
[27] S. Basu, G. Mukherjee, and A. Sonzogni, Nuclear Data Sheets **111**, 2555 (2010)
[28] B. Kharraja, S. S. Ghugre, U. Garg *et al.*, Phys. Rev. C **57**, 2903 (1998)
[29] J. M. Chatterjee, M. Saha-Sarkar, S. Bhattacharya *et al.*, Phys. Rev. C **69**, 044303 (2004)
[30] G. Li, X. Zhou, M. Liu *et al.*, Nucl. Instr. and Meth. A **1080**, 170804 (2025)
[31] D. Radford, Nucl. Instr. and Meth. A **361**, 297 (1995)
[32] B. Brown and W. Rae, Nucl. Data Sheets **120**, 115 (2014)
[33] A. Hosaka, K.-I. Kubo, and H. Toki, Nucl. Phys. A **444**, 76 (1985)
[34] M. Honma, T. Otsuka, T. Mizusaki *et al.*, Phys. Rev. C **80**, 064323 (2009)
[35] J. B. Moorhead and R. A. Moyer, Phys. Rev. **184**, 1205 (1969)
[36] P. Chowdhury, B. A. Brown, U. Garg *et al.*, Phys. Rev. C **32**, 1238 (1985)
[37] S. Sihotra, Z. Naik, S. Kumar *et al.*, Phys. Rev. C **83**, 024313 (2011)
[38] J. Cederkäll, G. Perez, M. Lipoglavek *et al.*, Z. Phys. A **359**, 227 (1997)
[39] B. Maheshwari and K. Nomura, Symmetry **14**, 2680 (2022)
[40] N. Nica, Nucl. Data Sheets **111**, 525 (2010)
[41] P. W. Zhao, Y. K. Wang, and Q. B. Chen, Phys. Rev. C **99**, 054319 (2019)
[42] D. Chen, J. Li, and R. Guo, Eur. Phys. J. A **59**, 142 (2023)
[43] J.-N. Zang, D. Chen, R. Guo *et al.*, Phys. Rev. C **112**, 034338 (2025)
[44] R. Guo, J. B. Lu, L. H. Zhu *et al.*, Phys. Rev. C **109**, 054309 (2024)
[45] P. W. Zhao, Phys. Lett. B **773**, 1 (2017)